

## Interaction between exsolution microstructures and magnetic properties of the magnetite-spinel solid solution

RICHARD J. HARRISON<sup>1</sup> AND ANDREW PUTNIS<sup>2</sup>

<sup>1</sup>Department of Earth Sciences, University of Cambridge, Downing Street, Cambridge CB2 3EQ, U.K.

<sup>2</sup>Institut für Mineralogie, Universität Münster, Corrensstrasse 24, D-48149 Münster, Germany

### ABSTRACT

Magnetic properties of exsolved samples of the  $(\text{Fe}_3\text{O}_4)_x(\text{MgAl}_2\text{O}_4)_{1-x}$  solid solution were measured over the temperature range 4–923 K and were correlated with microstructures observed by transmission electron microscopy. Several stages of microstructural development were identified. The early stages of exsolution are characteristic of spinodal decomposition with sinusoidal fluctuations in composition occurring parallel to {100}. Satellite peaks observed in both electron and X-ray diffraction patterns indicate an average wavelength for the fluctuations of 100 Å. Further development of this microstructure is characterized by an increasing amplitude of the fluctuations and a sharpening of the compositional profile. A fully exsolved sample produced at 700 °C consists of two phases with approximate compositions  $x = 0.19$  and  $x = 0.92$ .

Saturation magnetization ( $M_s$ ), saturation remanent magnetization ( $M_{rs}$ ), and coercivity ( $H_c$ ) were determined from hysteresis loops measured at temperatures in the range 4–300 K. Alternating-field susceptibility ( $\chi$ ) was measured at high temperatures up to 923 K. The temperature dependence of magnetic properties was found to be a complex function of the intrinsic properties of the homogeneous solid solution and the observed microstructure. A common feature of all exsolved samples is a pronounced decrease in  $M_s$  at temperatures below the Curie temperature of material with  $x < x_c$ , where  $x_c$  is the compensation point identified by Harrison and Putnis (1995). In the early stages of spinodal decomposition we observed samples with pronounced coercivity ( $H_c = 173$  mT) and unusually high remanence ( $M_{rs}/M_s = 0.82$ ) at 4 K, characteristic of magnetization reversal by strongly pinned conventional domain walls. At temperatures in the range 50–100 K the coercivity and remanence decrease rapidly, with hysteresis loops characteristic of magnetization reversal by weakly pinned interaction domain walls above 100 K. This transition in domain state is related to the development of paramagnetic boundaries around the Fe-rich components of the compositional fluctuations.

In the advanced stages of exsolution we observed coercivity and remanence more consistent with single-domain behavior. This is related to the sharpening of the compositional profile and the development of distinct lamellae with high shape anisotropy.

### INTRODUCTION

The interaction between magnetism and microstructure is arguably one of the most important mechanisms for increasing the stability of a natural remanent magnetization (NRM) over geological time. A wide range of microstructures exists in natural magnetic minerals associated with high-temperature oxidation (Tucker and O'Reilly 1980), cation ordering (Nord and Lawson 1989), spinodal decomposition (Smith 1980), and even lightning strikes (Banfield et al. 1994). A common cause of increased coercivity and remanence is the subdivision of large multidomain grains into fine-scale arrays of single-domain grains separated by exsolved lamellae of a non-magnetic phase. In natural titanomagnetite, for example, it is commonly proposed that exsolved lamellae of il-

menite, which are formed during oxidation at high temperatures, lead to enhanced remanence properties of the host spinel phase (Graham 1953; Larson et al. 1969; Strangway et al. 1968). Some workers suggest, however, that the scales of these oxidation-exsolution textures are too large to yield single-domain properties (for example, Hargraves and Banerjee 1973). A potential source of much finer-scale exsolution textures is subsolvus exsolution, which occurs in titanomagnetite at temperatures <500 °C (Price 1981). This phenomenon has been exploited for many years in the production of commercial permanent magnet materials (Livingston 1981). Typically exsolution occurs by a mechanism of spinodal decomposition, which yields a tweed-type microstructure consisting of sinusoidal fluctuations in composition with a

wavelength of  $\sim 100$  Å. Coarsening of this microstructure yields a fine-scale intergrowth of distinct magnetic and paramagnetic phases (Price 1980).

Although the titanomagnetite solid solution is the most important carrier of NRM in rocks, it is impossible to study the systematic development of subsolvus microstructures in synthetic titanomagnetite on a laboratory time scale because of the low temperatures required for exsolution (Price 1981). Our understanding of the magnetic consequences of spinodal decomposition in minerals is based on a few studies of natural material at relatively advanced stages of exsolution (Evans and Wayman 1974; Melnikov and Khisina 1976; Price 1980). However, it is possible to study the general behavior of magnetite-bearing solid solutions during the early stages of exsolution in related systems. We chose the solid solution between magnetite and spinel ( $\text{Fe}_3\text{O}_4$ )<sub>x</sub>( $\text{MgAl}_2\text{O}_4$ )<sub>1-x</sub> for this study because it is a mixture of magnetic and nonmagnetic end-members, there are large changes in Curie temperature as a function of composition across the solid solution, and there is a high-temperature solvus enabling the production of exsolution in synthetic samples on a laboratory time scale. In addition, spinel phases with bulk compositions within the  $\text{Fe}_3\text{O}_4$ - $\text{FeAl}_2\text{O}_4$ - $\text{MgFe}_2\text{O}_4$ - $\text{MgAl}_2\text{O}_4$  quadrilateral have recently been identified as fine-scale exsolution products in natural impure titanomagnetite (Krasnova and Krezer 1995). Therefore the magnetic properties of this solid solution are of both direct and indirect interest in rock magnetism.

The magnetic properties of the homogeneous solid solution have been studied previously (Harrison and Putnis 1995, 1996), and the variation in saturation magnetization, coercivity, and Curie temperature as a function of composition has been determined. This study presents an experimental characterization of synthetic samples of the magnetite-spinel solid solution that were annealed below the coherent solvus to yield a range of microstructures. Samples were investigated using a combination of magnetic hysteresis properties, high-temperature alternating-field susceptibilities, transmission electron microscopy, and X-ray diffraction. The results are interpreted on a qualitative basis, and the possible significance for natural magnetic minerals is discussed.

#### CRYSTAL AND MAGNETIC STRUCTURE OF THE HOMOGENEOUS SOLID SOLUTION

Magnetite ( $\text{Fe}^{2+}\text{Fe}_2^{3+}\text{O}_4$ ) and spinel ( $\text{MgAl}_2\text{O}_4$ ) are both cubic spinels with space group  $Fd\bar{3}m$  and eight formula units per unit cell. The 32 O atoms per unit cell are in an approximately close-packed arrangement with cations occupying eight tetrahedral (A) sites and 16 edge-sharing octahedral (B) sites. The partitioning of cations between octahedral and tetrahedral sites is temperature dependent, with cations ordering onto preferred sites at low temperatures and becoming increasingly disordered over the available sites at high temperatures. This process of non-convergent cation ordering ("nonconvergent" meaning there is no symmetry change) is discussed in detail in the

literature (for example, Carpenter et al. 1994; O'Neill and Navrotsky 1983) and leads to a complex distribution of cations between sites as a function of composition and temperature in the homogeneous solid solution (Nell and Wood 1989; Sack and Ghiorso 1991). The homogeneous solid solution is unstable with respect to an intergrowth of  $\text{MgAl}_2\text{O}_4$ -rich and  $\text{Fe}_3\text{O}_4$ -rich phases at temperatures  $< 1000$  °C, leading to exsolution. For more detailed background information on cation ordering and exsolution processes in minerals, see Putnis (1992).

The spin-only magnetic moments associated with  $\text{Fe}^{2+}$  and  $\text{Fe}^{3+}$  ions are 4 and 5  $\mu_B$ , respectively ( $1 \mu_B = 9.27 \times 10^{-24}$  Am<sup>2</sup>). Below the Curie temperature ( $T_C$ ) of a magnetic spinel, Fe atoms on B sites have their moments aligned parallel to each other but antiparallel to those on A sites. The net saturation magnetization is given by the difference between the octahedral and tetrahedral sublattice magnetizations (for example, Stephenson 1972). The trend in saturation magnetization as a function of composition in samples quenched from 1400 °C was determined by Harrison and Putnis (1995). For compositions  $x > 0.3$  ( $x$  is the mole fraction of magnetite) the solid solution is ferrimagnetic with the B sublattice magnetization greater than the A sublattice magnetization. For compositions  $x < 0.3$  the solid solution is ferrimagnetic with the A sublattice magnetization greater than the B sublattice magnetization. The composition  $x_c = 0.3$  is a compensation point at which the net magnetization is zero (antiferromagnetic). The position of  $x_c$  is controlled by the cation distribution and hence is a function of temperature and kinetics. The cation distribution was calculated as a function of temperature and composition (Harrison and Putnis 1995) with the use of the thermodynamic model of Nell and Wood (1989). These calculations suggest that  $x_c$  moves toward the magnetite end-member when the solid solution is annealed at progressively lower temperatures. Consequently, we expect  $x_c$  to be  $> 0.3$  in this study because the samples were annealed at temperatures lower than the apparent equilibration temperature of samples quenched from 1400 °C ( $\sim 900$ – $1000$  °C; Wood et al. 1986).

#### EXPERIMENTAL AND ANALYTICAL PROCEDURES

##### Sample synthesis and annealing

The synthesis of all samples used in this study is described in detail by Harrison and Putnis (1995). The starting materials for all syntheses were 99.9% pure  $\text{Fe}_2\text{O}_3$  and  $\text{MgO}$ , and  $\text{Al}_2\text{O}_3$  prepared by firing  $\text{AlCl}_3 \cdot 6\text{H}_2\text{O}$  for 2 h at 400 °C, 5 h at 700 °C, and 1 h at 900 °C. The oxides were weighed in stoichiometric proportions, ground together, and pressed into pellets. The pellets were then fired at 1400 °C for periods between 3 and 5 d in a vertical-tube gas-mixing furnace under controlled  $f_{\text{O}_2}$  (Nafziger et al. 1971). A value of  $\log f_{\text{O}_2} = -4.2$  was chosen to yield stoichiometry in the magnetite component of the solid solution (Dieckmann 1982). Samples were quenched from 1400 °C by dropping directly from the furnace into water.

Samples with bulk compositions  $x = 0.51$  and  $x = 0.61$  were used as starting material for the low-temperature annealing experiments (samples SP12 and SP13 from Harrison and Putnis 1995). Annealing was performed at 630 and 700 °C in a gas-mixing furnace. Samples were suspended in open platinum tubes and quenched directly into water at the end of the experiment. The value of  $f_{O_2}$  was controlled by the mixing of CO<sub>2</sub> and H<sub>2</sub> gases using Tylan General FC-260 gas-flow controllers. An estimate of the  $f_{O_2}$  for stoichiometric magnetite was made by extrapolating the high-temperature results of Dieckmann (1982), and the ratio of CO<sub>2</sub> to H<sub>2</sub> was set accordingly (Deines et al. 1974). However, the rate of reaction of these gases is low at 700 °C, and it is unlikely that the equilibrium  $f_{O_2}$  was reached.

Some annealing experiments were performed on samples sealed under vacuum in quartz tubes. It was found that the rates of exsolution were at least an order of magnitude slower under vacuum than under a CO<sub>2</sub>-H<sub>2</sub> atmosphere. This observation suggests that small departures from stoichiometry may have occurred during the gas-mixing experiments, leading to an increase in the defect population and enhanced diffusion kinetics (Dieckmann and Schmalzried 1977). Although this is undesirable from the point of view of correlating the behavior of exsolved samples with that of the stoichiometric solid solution, these conditions were necessary to produce exsolution on a reasonable time scale. A summary of all annealing experiments is given in Table 1.

### TEM and XRD characterization

Samples were prepared for TEM investigation by ion-beam thinning sintered chips mounted on a carbon grid. The microscope was operated at 100 kV, and bright-field imaging was used throughout. Powder XRD traces were recorded using an automated step-scan diffractometer in reflection geometry (CuK $\alpha$  radiation). The diffractometer was fitted with a diffracted-beam monochromator, which reduces the background caused by fluorescence of Fe-rich samples. Both CuK $\alpha_1$  and CuK $\alpha_2$  components were present in the traces.

### Low-temperature hysteresis measurements

Magnetic hysteresis loops were measured at temperatures in the range 4–300 K using an Oxford Instruments vibrating sample magnetometer equipped with a superconducting magnet. Sintered polycrystalline pellets with masses in the range 10–40 mg were placed on the end of a plastic sample holder and held in place with PTFE tape. The temperature was controlled by balancing the flow of helium gas through the magnet bore with a small resistive heater. Hysteresis loops were recorded at various field ramp rates in the range 5–20 mT/s and up to maximum fields between 1 and 3 T. The saturation magnetization ( $M_s$ ) was extracted from the loops by fitting the high-field portion with an equation of the form  $M = M_s (1 - a/H - b/H^2) + cH$  using a least-squares procedure (Brown et al. 1993). The linear term in this equation accounts for

TABLE 1. Conditions used during annealing experiments

Sample	Bulk composition ( $x^*$ )	$T$ (°C)	CO <sub>2</sub> /H <sub>2</sub> (%)	$t$ (d)	Observed microstructure**
e20	0.61	700	96	19	A
e24	0.51	630	94	19	B
e25	0.61	630	94	19	C
e26	0.51	630	94	40	B
e27	0.61	630	94	40	C

\* Composition defined according to the ideal formula (Fe<sub>3</sub>O<sub>4</sub>)<sub>x</sub>(MgAl<sub>2</sub>O<sub>4</sub>)<sub>1-x</sub>.  
 \*\* A = Incoherent intergrowth of rounded precipitates; abundant moiré fringes. B = Early-stage spinodal microstructure; modulations parallel to {100},  $\lambda = 100$  Å. C = Coarsened spinodal microstructure; coherent lamellae parallel to {100}.

the presence of paramagnetic material in the samples. Coercivity ( $H_c$ ) and saturation remanent magnetization ( $M_{rs}$ ) were taken directly from the loops. Details of a similar study of the homogeneous solid solution were given by Harrison and Putnis (1995).

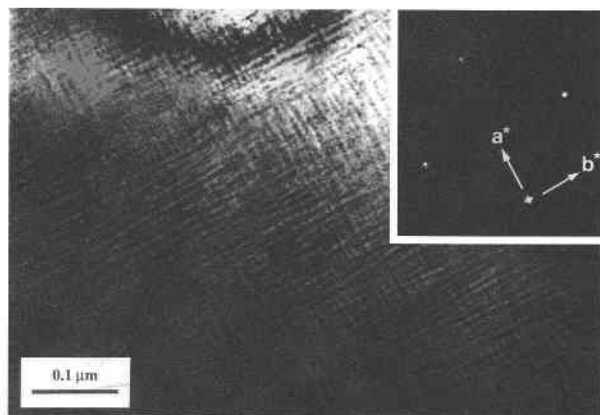
### High-temperature susceptibility measurements

Measurements of high-temperature alternating-field susceptibility ( $\chi$ ) were made in air using a KAPPA susceptibility bridge. Individual pellets of sintered polycrystalline material with masses ranging from 18 to 38 mg were placed in an open test tube inside a water-cooled furnace. Measurements of susceptibility were made every 15 to 20 s while the temperature was ramped from room temperature to 650 °C and back again at a rate of 11 °C/min. Temperatures were measured with a Pt-Rh thermocouple, which was placed directly next to the sample. The total time for each experiment was ~1.9 h. Details of a similar study of the homogeneous solid solution were given by Harrison and Putnis (1996).

### RESULTS OF TEM AND XRD CHARACTERIZATION

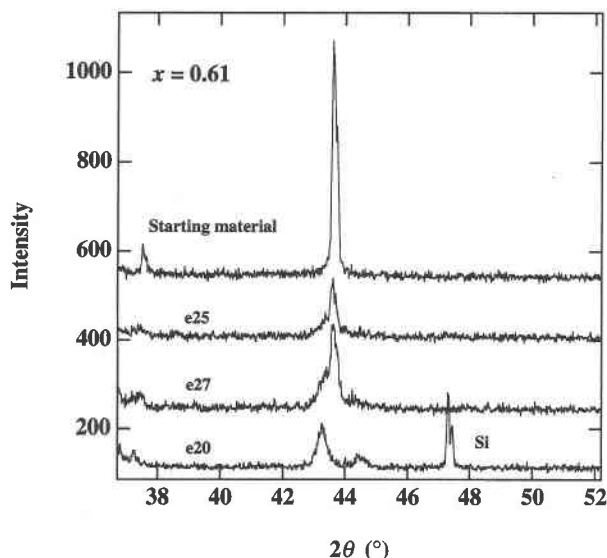
The microstructure observed in samples e24 and e26 (bulk composition  $x = 0.51$ , Table 1) consists of fine-scale modulations parallel to {100}. A bright-field micrograph of e24 taken with the electron beam parallel to [100] is shown in Figure 1 with the corresponding selected-area diffraction pattern (SAED) inset. Each reciprocal lattice point in the diffraction pattern shows well-developed satellite intensity parallel to  $a^*$ . This can also be seen in the XRD traces of samples e24 and e26 shown in Figure 2. The satellite intensity does not form distinct reflections around the Bragg peak, so it is not possible to define a unique wavelength for the modulation. The position of the maximum satellite intensity in reciprocal space was estimated from digitized images of the electron diffraction patterns. This gave a wavelength of 100 Å, which is in excellent agreement with estimates measured directly from the micrographs. This microstructure is characteristic of spinodal decomposition (Smith 1980; Buseck et al. 1980).

Figure 3 shows the development of the 400 Bragg reflection in samples with bulk composition  $x = 0.61$  an-



**FIGURE 1.** Bright-field electron micrograph of sample e24, showing compositional modulations developed parallel to  $\{100\}$ . Inset is the selected-area diffraction pattern of sample e24 recorded with the electron beam parallel to  $[001]$ . Diffraction spots have a distinctive cross shape, which is characteristic of tweed-textures produced by spinodal decomposition.

nealed at different temperatures and times. The peak profile of samples e25 and e27 shows a central peak, corresponding to the position of the 400 reflection in the starting material, and a second peak on the low-angle side, corresponding to a more Fe-rich phase. The position of this second peak is the same in both samples, which implies that the amplitude of the compositional fluctuation had not changed during the additional annealing period. An example of the microstructure seen in e25 is shown in Figure 4a. An SAED pattern taken with the



**FIGURE 3.** Comparison of the XRD 400 peak profiles of samples SP13 (starting material), e25, e27, and e20. The additional peak near  $47.4^\circ$   $2\theta$  in sample e20 is due to the internal Si standard.

electron beam parallel to  $[1\bar{3}0]$  is shown in Figure 4b. The fluctuations in composition are more defined than in Figure 1, with distinct lamellae developed parallel to  $\{100\}$  in some areas. The electron diffraction pattern shows streaking parallel to  $a^*$ , indicating that the microstructure had not fully developed into an intergrowth of two distinct phases. The evidence suggests that samples e25 and e27 are in the latter stages of coherent exsolution by a mechanism of spinodal decomposition. This stage is reached when the amplitude of the compositional fluctuation reaches the limbs of the coherent solvus. Exsolution then proceeds by the gradual transformation of the compositional profile from a sine-wave to a square-wave morphology (Hilliard 1970). Further evidence for this inter-

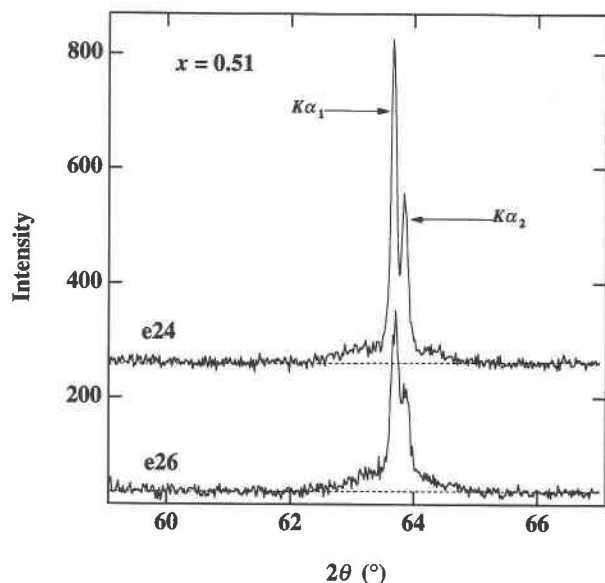


**FIGURE 2.** Comparison of the XRD 440 peak profiles of samples e24 and e26 (solid lines). Dashed lines are the results of a least-squares fit to the background intensity well away from the Bragg peaks. The profiles clearly show the development of satellite intensity around the base of each peak.

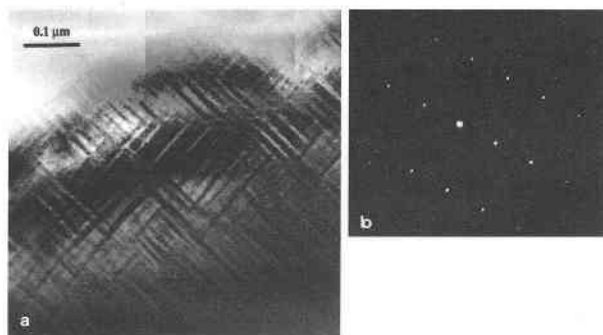


**FIGURE 4.** (a) Bright-field electron micrograph of sample e25, showing the development of straight-sided compositional modulations parallel to  $\{100\}$ . (b) Selected-area diffraction pattern of sample e25, recorded with the electron beam parallel to  $[130]$ .

pretation can be obtained from the magnetic properties and is discussed in a later section.

The microstructure of sample e20 is quite different from that of any of the samples annealed at 630 °C. Two micrographs are shown in Figures 5a and 5b, and a typical SAED pattern taken with the beam parallel to [100] is shown in Figure 5c. The electron diffraction pattern in all cases studied is the superposition of two cubic spinel reciprocal lattices with  $a^*$  axes parallel. Typically, the microstructure in this sample is obscured by sets of moiré fringes, which occur throughout the specimen (Fig. 5a). Moiré fringes are a consequence of double diffraction from two overlapping phases that either have slightly different lattice spacings or are slightly rotated with respect to each other (Hirsch et al. 1965; McLaren 1991). If the sample is tilted so that double diffraction does not occur, then the two-phase microstructure becomes clearer (Fig. 5b). The microstructure consists of rounded precipitates of one phase within a matrix of the second. The lack of a lamellar microstructure suggests that the interface between exsolved phases is incoherent and is not associated with a large lattice strain. It is likely that the mechanism of exsolution in this case was nucleation and growth. The compositions of coexisting phases in an incoherent intergrowth are given by the limbs of the chemical solvus, which lie outside the limbs of the coherent solvus. The difference in composition between coherent and incoherent intergrowths can clearly be seen from the relative position of the low-angle Fe-rich peaks in Figure 3.

The XRD trace of sample e20 was recorded between 10 and 70° 2 $\theta$  with an internal Si standard (Fig. 3). The peak positions of the Fe-rich and Fe-poor phases were measured from the traces and corrected for the positions of three Si peaks. The lattice parameter for each phase was then determined using a standard least-squares procedure. This yielded lattice parameters of 8.375(2) and 8.154(2) Å for the Fe-rich and Fe-poor phases, respectively. The number in parentheses is the standard deviation in the final decimal place calculated by the least-squares program. The true error is probably larger than this because of the low number of peaks used in the refinement (seven for the Fe-rich phase and five for the Fe-poor phase).

Taking these lattice parameters at face value we may estimate the compositions of the two phases by using the calibration of lattice parameter vs. composition given by Harrison and Putnis (1995). This yields  $x = 0.92$  and  $x = 0.19$  for the Fe-rich and Fe-poor phases, respectively, with an estimated error of  $\pm 0.03$ . These values are significant only if the solid solution exsolves along the binary join between  $\text{Fe}_3\text{O}_4$  and  $\text{MgAl}_2\text{O}_4$ . Exsolution in this system occurs within the quaternary solid solution between  $\text{Fe}_3\text{O}_4$ ,  $\text{FeAl}_2\text{O}_4$ ,  $\text{MgFe}_2\text{O}_4$ , and  $\text{MgAl}_2\text{O}_4$ . The compositions of coexisting phases within this quaternary have been modeled (Lehmann and Roux 1986). Although there is a possibility that the  $\text{MgAl}_2\text{O}_4$ -rich and  $\text{Fe}_3\text{O}_4$ -rich phases of the intergrowth contain small components of  $\text{FeAl}_2\text{O}_4$  and  $\text{MgFe}_2\text{O}_4$ , the results of Lehmann and Roux

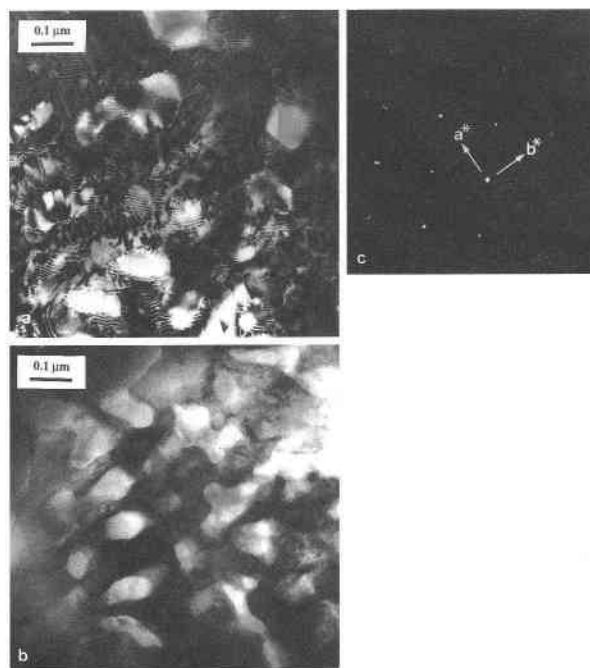


**FIGURE 5.** (a) Bright-field electron micrograph of sample e20, showing moiré fringes caused by the double diffraction from overlapping phases of slightly different lattice spacing. (b) Bright-field electron micrograph of sample e20, with the specimen tilted to reduce the formation of moiré fringes. The exsolved phases have a rounded morphology, consistent with incoherent exsolution. (c) Selected-area diffraction pattern of sample e20, recorded with the electron beam parallel to [001]. The diffraction pattern is the superposition of two cubic spinel reciprocal lattices with cubic axes parallel.

(1986) suggest that tie lines between exsolved phases remain near the  $\text{Fe}_3\text{O}_4$ - $\text{MgAl}_2\text{O}_4$  join if, as in this case, the bulk composition is near the center of the  $(\text{Fe}_3\text{O}_4)_x(\text{MgAl}_2\text{O}_4)_{1-x}$  solid solution.

## RESULTS OF MAGNETIC CHARACTERIZATION

### High-temperature susceptibility measurements

The relative stages of microstructural development observed by TEM can be illustrated further by measurements of high-temperature alternating-field susceptibility, which are sensitive to the state of local order and composition. Results for samples e26, e27, and e20 are shown in Figure 6. The  $\chi$ - $T$  curves are nonreversible because of additional exsolution and cation ordering, which occurs at temperatures  $>300$ – $400$  °C. Each starting material has a microstructure and degree of cation order that is metastable with respect to the equilibrium state consisting of an incoherent intergrowth of two phases with compositions on the chemical (strain-free) solvus. Therefore, as the samples are heated in the susceptibility bridge there is a driving force for both cation ordering and exsolution. The rate of exsolution is surprisingly fast in these experiments. As the samples are heated in air the rim of the sintered pellets may become slightly oxidized, leading to

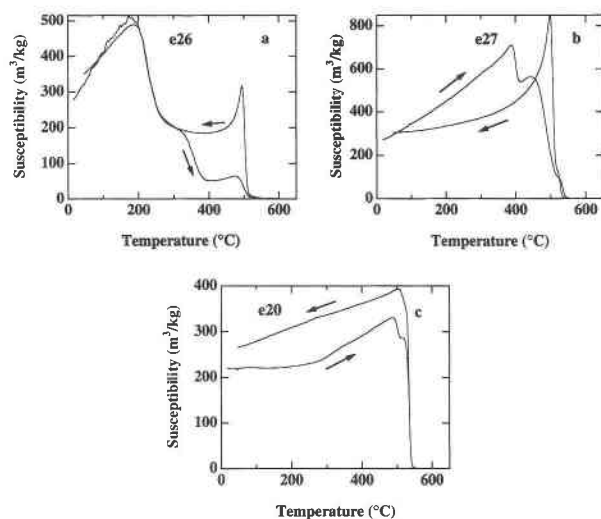


FIGURE 6. Alternating-field susceptibility vs. temperature for samples (a) e26, (b) e27, and (c) e20. Arrows indicate the directions of heating and cooling.

enhanced diffusion rates near the surface of the sample. The effect is more pronounced in Fe-rich material with  $x \geq 0.55$ . A more detailed discussion of these effects was given by Harrison and Putnis (1996).

The microstructure of sample e26 consists of fine-scale modulations parallel to  $\{100\}$  with wavelength of  $\sim 100$  Å, consistent with the early stages of spinodal decomposition. At some temperature,  $T$ , this material consists of magnetically ordered regions, with  $T_c > T$ , surrounded by paramagnetic regions, with  $T_c < T$ . The size of each magnetic region is less than the critical size for uniform single-domain behavior ( $\sim 600$ – $800$  Å; Newell et al. 1993), and hence the material can be considered as a nondilute array of interacting single-domain particles. The  $\chi$ - $T$  curve (Fig. 6a) shows a broad hump with a maximum at  $\sim 200$  °C. This hump is caused by the transition to superparamagnetic behavior in the single-domain particles (unblocking). Below 200 °C the mutual magnetostatic interaction between particles produces long-range magnetic alignment. Above 200 °C the alignment breaks down because thermal excitations provide enough energy for each single-domain particle to overcome the anisotropy and interaction fields. At temperatures  $>300$  °C the  $\chi$ - $T$  curve becomes complicated by rapid nucleation and growth of the equilibrium Fe-rich phase. This phase produces a distinct Hopkinson peak on cooling through 520 °C (Dunlop 1974). The Hopkinson peak results from thermal enhancement of magnetic susceptibility near  $T_c$  and from competition between the decreasing magnetic anisotropy and magnetization as  $T$  approaches  $T_c$ . Exsolution does not proceed to completion in this sample, and a strong magnetic signal from the original coherent intergrowth remains on cooling. Similar behavior is seen in homogeneous starting material of the same bulk composition (Harrison and Putnis 1996).

The microstructure in sample e27 is at a more ad-

vanced stage than that in e26, with distinct lamellae developed in some areas. This, together with the XRD evidence in Figure 3, implies that the amplitude of the compositional fluctuation reached the limbs of the coherent solvus and that the profile began the transition from sine-wave to square-wave form. The  $\chi$ - $T$  curve (Fig. 6b) displays a sharp drop at about 400 °C followed by complex behavior above this temperature because of nucleation and growth of the equilibrium phase. The drop at 400 °C corresponds to the  $T_c$  of the metastable coherent phase. This phase is significantly poorer in Fe in comparison with the equilibrium incoherent phase and therefore has a lower  $T_c$ . The difference in composition is a result of the coherency-strain contribution to the free energy of the solid solution (Putnis 1992). The equilibrium incoherent phase produces a large Hopkinson peak on cooling through 520 °C. In this case there is no magnetic signal from the original coherent intergrowth, indicating that growth of the incoherent phase proceeded to completion.

The microstructure of sample e20 consists of an incoherent intergrowth of two phases of distinct composition, which suggests equilibrium was reached during the 700 °C annealing experiment. The  $\chi$ - $T$  curve (Fig. 6c) displays a drop at 500 °C followed by a small shoulder and a sharp drop at about 550 °C. The shoulder in the  $\chi$ - $T$  curve could be caused by a change in the cation distribution of the magnetite-rich phase. There is a large interaction between the degree of cation order and  $T_c$  in this system (Harrison and Putnis 1996). The first and second drop in  $\chi$  would then correspond to  $T_c$  for a degree of cation order representing equilibrium at 700 and 550 °C, respectively. Alternatively, the change in  $T_c$  could be caused by nucleation of a phase with composition shifted to the position of the chemical solvus at 550 °C. It is not possible to extract compositional information from these results unless the interaction between cation order and  $T_c$  is determined in detail. However, it is interesting that the composition of the Fe-rich phase derived from XRD ( $x \approx 0.92$ ) yields  $T_c = 527$  °C, using the calibration of  $T_c$  vs.  $x$  derived by Harrison and Putnis (1996). This is in good agreement with the susceptibility measurements.

#### Temperature dependence of $M_s$

The variation of  $M_s$  vs. temperature in samples e20, e25, e26, and e27 is shown in Figure 7. All samples show a distinct decrease in  $M_s$  at temperatures  $<75$ – $125$  K. This behavior can be understood by combining the known variation of  $M_s$  and  $T_c$  as a function of composition in the solid solution (Harrison and Putnis 1995, 1996) with the distribution of compositions throughout space in the exsolved samples (i.e., the compositional profile). The general principle can be illustrated using e26 as an example. This sample has a microstructure consistent with the early stages of spinodal decomposition, and therefore the compositional profile can be approximated by sinusoidal fluctuations with a wavelength of about 100 Å. The change in composition and  $T_c$  as a function of distance

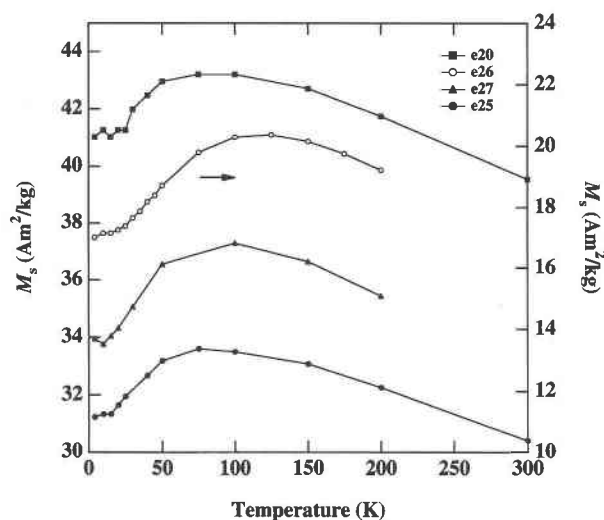


FIGURE 7. Saturation magnetization,  $M_s$ , vs. temperature for samples (from top to bottom) e20, e26, e27, and e25. The left scale corresponds to samples e25, e27, and e20 ( $x = 0.61$ ). The right scale corresponds to sample e26 ( $x = 0.51$ ).

in the exsolved material is illustrated schematically in Figure 8. Arrows indicate the direction and magnitude of the tetrahedral (A) and octahedral (B) sublattice magnetizations. The dashed line indicates the position of the compensation point  $x = x_c$ . At a sufficiently low temperature the entire specimen becomes magnetically ordered with the A moments aligned antiparallel to the B moments (Fig. 8a). Regions with composition  $x > x_c$  have a net magnetization that is parallel to the B sublattice magnetization (designated the positive direction). Regions with composition  $x < x_c$  have a net magnetization that is antiparallel to the B sublattice magnetization (the negative direction). This leads to partial compensation of the bulk saturation magnetization. As the temperature increases, the reversed component of the compositional fluctuation becomes paramagnetic (Fig. 8b), and the bulk saturation magnetization increases to a maximum. As the temperature further increases, the positively magnetized components become paramagnetic, leading to a gradual decrease in saturation magnetization as room temperature is approached. The saturation magnetization eventually reaches zero at the  $T_c$  for the most Fe-rich component of the compositional fluctuation.

The temperature at which the maximum  $M_s$  occurs ( $T_{max}$ ) depends on three factors. First, it depends on the value of  $T_c$  at the compensation point. This places an upper limit on  $T_{max}$ . Second, as the sample cools below this upper limit the magnetization decreases only when the acquisition of negative magnetization exceeds the increase in positive magnetization resulting from enhanced magnetic order. Therefore, the position of  $T_{max}$  results from competition between the rates of positive and negative magnetic ordering and is always lower than the  $T_c$  corresponding to  $x = x_c$ . Third,  $T_{max}$  is sensitive to the shape of the compositional profile because the profile af-

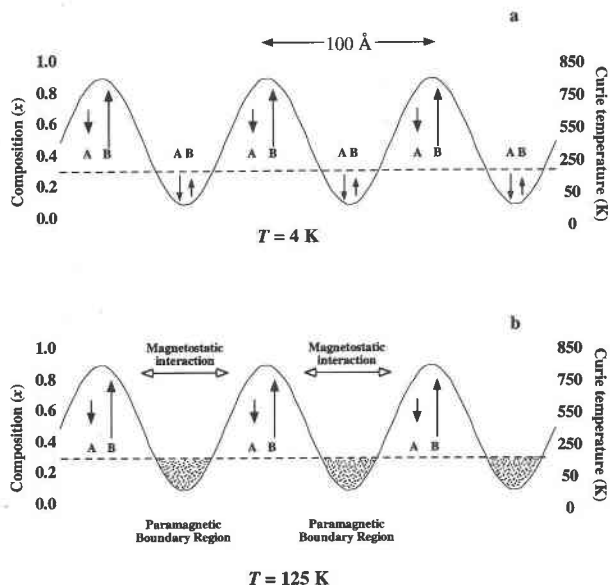


FIGURE 8. Schematic illustration of the variations in composition ( $x$ ) and Curie temperature (K) with distance in sample e26. The curve represents a sinusoidal fluctuation in composition with wavelength 100 Å. Arrows indicate the direction and magnitude of the tetrahedral (A) and octahedral (B) sublattice magnetizations at various positions along the compositional profile for temperatures of (a) 4 K and (b) 125 K. The dashed line indicates the approximate position of the compensation point. The dotted regions in b indicate paramagnetic regions of the material that have Curie temperatures  $< 125$  K.

fects which compositions are present in the sample and their relative amounts. This last point can be illustrated by comparing samples e20 ( $T_{max} \approx 75$  K) and e26 ( $T_{max} \approx 125$  K). Sample e20 is completely exsolved into two phases of distinct composition. The compositional profile is therefore square rather than sinusoidal. This means that the amount of material with composition other than the two equilibrium compositions is exactly zero, and  $M_s$  decreases only at temperatures below the  $T_c$  of the Fe-poor phase ( $\sim 75$  K in this case). Sample e26 contains fractions of material over a wide range of compositions close to the compensation point, and hence  $T_{max}$  is much closer to the theoretical upper limit. Sample e25 has  $T_{max} \approx 75$  K, which indicates that it contains less material with composition close to the compensation point than does e26. This reflects both the difference in bulk composition and the squarer compositional profile inferred from TEM and XRD.

The above discussion implies that  $T_c$  at the compensation point is  $> 125$  K. Harrison and Putnis (1996) gave  $T_c$  at  $x = x_c$  between 20 and 50 K. The apparent discrepancy is due to the fact that the samples used in the present study were annealed at low temperatures, whereas the calibration of  $T_c$  vs.  $x$  by Harrison and Putnis (1996) used samples quenched from 1400 °C. This has two consequences. First, the position of  $x_c$  moves to more Fe-rich compositions in samples annealed at low temperatures be-



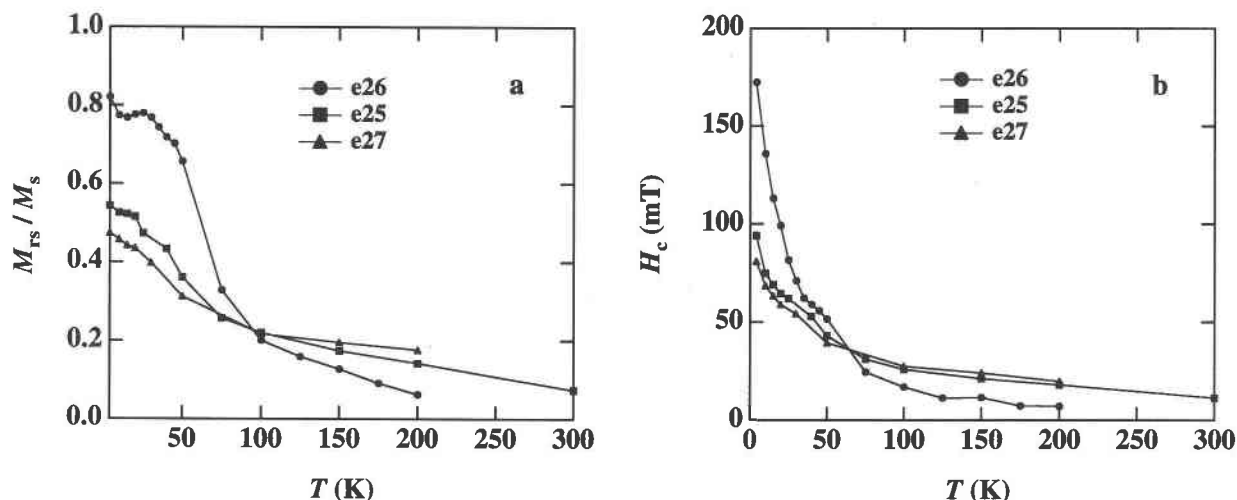


FIGURE 9. (a) Ratio of saturation remanent magnetization to saturation magnetization,  $M_{rs}/M_s$ , vs. temperature, and (b) coercivity,  $H_c$ , vs. temperature for samples e26 (circles), e25 (squares), and e27 (triangles).

cause of the change in distribution of Fe cations between octahedral and tetrahedral sites (Nell and Wood 1989). Second,  $T_c$  is strongly dependent on the degree of cation order (Harrison and Putnis 1996). This can cause  $T_c$  to be up to 70 °C higher in samples annealed at low temperatures than in the same material quenched from 1400 °C. Hence, it is not possible to extract any compositional information from the  $M_s$ - $T$  curves unless the  $T_c$ - $x$  curve is recalibrated for samples equilibrated at the appropriate annealing temperature.

The large difference in  $M_s$  among samples e25, e27, and e20 reflects the different amplitudes and shapes of their compositional profiles and can be correlated with the  $\chi$ - $T$  curves discussed earlier (Fig. 6). The microstructure observed in e20 is consistent with incoherent exsolution resulting from a nucleation and growth mechanism. The compositions of coexisting phases derived from XRD ( $x = 0.19$  and  $x = 0.92$ ) correspond to the limbs of the chemical solvus.  $M_s$  is highest in this sample because it contains the largest possible fraction of Fe-rich material. The microstructures observed in e25 and e27 are consistent with coherent exsolution resulting from a mechanism of spinodal decomposition. The amplitude of the compositional fluctuation in this case is given by the position of the coherent solvus with  $x < 0.92$ , and  $M_s$  is significantly lower than for an incoherent intergrowth. The difference in  $M_s$  between samples e25 and e27 implies a higher fraction of Fe-rich material in e27. Given that the amplitude of the compositional profile of both samples reaches the coherent solvus, the increased magnetization reflects the changing shape of the profile (i.e., the transition from sine-wave to square-wave morphology is more advanced in e27).

#### Temperature dependence of magnetic domain state

The temperature dependencies of  $M_{rs}/M_s$  and  $H_c$  in samples e25, e26, and e27 are shown in Figure 9. It was not

possible to determine these parameters for e20 because the high-field ramp rate used to record hysteresis loops for this sample (20 mT/s) caused time-dependent magnetization effects that affected the measurements at low fields. A ramp rate of 5 mT/s was used for all other samples. The hysteresis properties can be interpreted in terms of the changes in magnetic domain state that occur as a function of microstructure and temperature. Many important advances in the theory of domain structures have been made in the past decade (for a review, see Merrill and Halgedahl 1995). Micromagnetic calculations show that for an equidimensional magnetic particle of linear dimension  $< 600$  Å the magnetization is essentially uniform throughout the particle volume (single-domain state). For particles  $> 600$ – $800$  Å the magnetization exists in a vortex state that is highly nonuniform throughout the entire particle volume (Newell et al. 1993). In much larger particles ( $> 1$  μm) these vortex states yield to more conventional multidomain states, i.e., several uniformly magnetized grains separated by Bloch walls.

The microstructures investigated here pose several difficulties when considering the possible domain states and magnetic structures that might exist. First, the shapes of the intergrown phases are not always equidimensional (Fig. 4a), which means that the relationship between particle size and domain state is not strictly defined. Second, residual stresses are thought to be very important in determining domain state (Worm et al. 1991). High stresses would be present in samples e26, e25, and e27 because of the coherency of the intergrown phases. This may affect coercivity directly through magnetostriction (Shive and Butler 1969) or indirectly through its effect on the domain state. Third, the very fine scale of the exsolution microstructures means that there is strong interaction between magnetic particles, which complicates the comparison between the observed behavior and the calculated behavior based on isolated particles. In particular, the de-



magnetizing effects of magnetic poles on the surfaces of nonmagnetic lamellae have to be considered. For these reasons the interpretation of the experimental data in terms of changes in domain state is kept at a simple and qualitative level.

At all temperatures  $>100$  K the coercivity and remanence of sample e26 is low, and the hysteresis loops are characteristic of multidomain magnetization reversal as shown in Figure 10a. At these temperatures the sample consists of magnetite-rich regions surrounded by paramagnetic boundary regions as illustrated previously in Figure 8b. Conventional magnetic domain walls (Bloch walls) cannot exist in this material because each magnetic region is below the threshold size for uniform single-domain behavior (Newell et al. 1993). However, because of the extremely fine scale of the microstructure, there is a large interaction between adjacent magnetic regions, which can lead to the formation of interaction domains (Bates et al. 1962; Craik and Isaac 1960). Interaction domains arise in nondilute arrays of single-domain particles when the mutual interaction between particles causes long-range magnetic alignment. Within each interaction domain many single-domain particles are magnetized in the same direction. Adjacent domains are separated by an interaction domain wall where the magnetic alignment of single-domain particles reverses abruptly. We suggest that the hysteresis properties in this material at temperatures  $>100$  K result from the motion of interaction domain walls. These walls are weakly pinned, resulting in low coercivity and remanence.

At high temperatures the width of the paramagnetic boundary regions is large, and the interaction between magnetic particles is mainly magnetostatic. When the temperature decreases the width of the paramagnetic regions decreases smoothly as more Fe-poor material is cooled through the appropriate  $T_c$ . This increases the exchange contribution to the particle interaction as the connectivity of magnetic regions increases. At some temperature the sample cools below the  $T_c$  of all components in the compositional fluctuation, and the whole crystal becomes magnetically ordered (Fig. 8a). Conventional domain walls are then possible. The transition from interaction domain walls to conventional domain walls occurs at about 100 K in sample e26 and is responsible for a large increase in remanence below this temperature (Fig. 9a). A hysteresis loop recorded at 4 K is shown in Figure 10b. The sample saturates in a field of 1 T. As the field is reduced there is very little reduction in magnetization, resulting in values of  $M_r/M_s$  up to 0.82. The coercivity is 3.75 times higher than the coercivity of a homogeneous sample with the same bulk composition (Harrison and Putnis 1995), implying that there is considerable resistance to the motion of domain walls through the crystal.

The behaviors of samples e25 and e27 are qualitatively similar to that of sample e26. However, the maximum coercivity and remanence in these samples at  $<100$  K are much less than those observed in e26. Conversely, the coercivity and remanence at  $>100$  K are greater than in

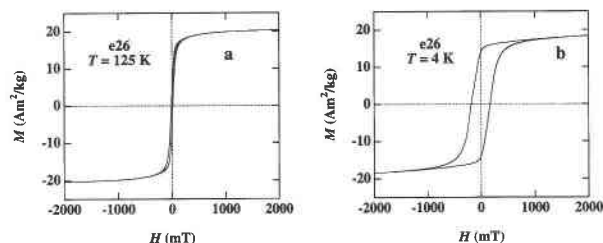


FIGURE 10. Magnetization,  $M$ , vs. field,  $H$ , for sample e26 at (a) 125 K and (b) 4 K.

e26. Physically these samples differ from e26 in two ways. First, they have different bulk compositions (Table 1) and contain a higher percentage of Fe-rich material. Second, exsolution is at a more advanced stage in these samples, as discussed earlier. The enhanced remanence properties at temperatures  $>100$  K in these samples indicate increased single-domain character in the magnetite-rich regions of the compositional fluctuations. This is probably caused by the gradual transition from a sinusoidal to a square compositional profile and the development of discrete lamellae with significant shape anisotropy (Fig. 4a). The gradual coarsening of fine-scale exsolution textures with a cubic morphology to more lamellar microstructures has been previously recognized in natural titanomagnetite (Price 1980). For reasons outlined in the next section it is only possible to speculate about the pinning mechanisms that operate at temperatures below which the sample becomes completely magnetized. The lower coercivity and remanence observed in samples e25 and e27 at  $<100$  K may reflect a difference in the pinning force experienced by domain walls in an intergrowth with sharp interfaces in comparison with an intergrowth with more diffuse interfaces. Alternatively, it may reflect the higher proportion of Fe-rich to Fe-poor material in these samples. The possibility that domain-wall formation is inhibited in this material, leading to single-domain properties even at low temperatures, is discussed in the next section.

### Origin of high remanence at low temperatures

To assess the possible pinning mechanisms that might operate in this material, it is necessary to discuss the possible width of the conventional domain walls that exist at  $<100$  K. The width of a domain wall results from the competition between the exchange constant ( $A$ ) and the anisotropy constant ( $K$ ) and is given by the equation  $w = \pi\sqrt{A/K}$ . Materials with large exchange constants (and consequently high  $T_c$ ) have wide domain walls, typically 500–1000 Å in Fe-rich solid solutions. Materials with small exchange constants (i.e., low  $T_c$ ) or high anisotropy have thin domain walls (e.g., 10–100 Å). It is not possible to calculate the width of domain walls in this case without detailed knowledge of the compositional and temperature dependence of exchange and anisotropy constants in the solid solution.

The width of the domain wall affects how efficiently

it is pinned by stress fields of a particular wavelength (Xu and Merrill 1989). In this case the important length scale is the wavelength of the compositional fluctuations ( $\lambda \approx 100 \text{ \AA}$ ). If  $w \gg 100 \text{ \AA}$ , then there is little interaction between the wall and fluctuations in stress. Maximum pinning occurs when  $w \approx \lambda/5$  (Xu and Merrill 1989). If thin walls exist in this material they would be pinned at the Fe-poor regions of the compositional fluctuation, where  $A$  is at a minimum and the coercivity is maximum (Harrison and Putnis 1995). Quantitative analysis of the effect of stress on the domain-wall energy requires knowledge of the temperature and compositional variation in the magnetostriction constants. The effect of stress on the orientation of magnetic moments and the structure of the domain wall must also be assessed. In addition to the effect of stress, the walls also experience a pinning force caused by the variation in  $A$  and  $K$  as a function of distance through the material (Zijlstra 1982). Fluctuations in these quantities cause the wall energy to vary as a function of distance, resulting in a pinning force that again depends on the relative size of  $w$  and  $\lambda$ .

An alternative explanation for the low-temperature behavior is possible if the presence of fluctuations in composition actually inhibit the formation of conventional domain walls. This would produce material with single-domain properties at temperatures below which the material is completely magnetized. This type of behavior has been suggested previously to explain the unusual behavior of stoichiometric coarse-grained titanomagnetite that shows superparamagnetic behavior at room temperature and single-domain behavior at lower temperatures, despite having grain sizes well within the multidomain field (Deutsch et al. 1981). The ideal ratio  $M_r/M_s$  in an array of randomly oriented single-domain particles is 0.5 (Dunlop 1981). Both samples e25 and e27 have  $M_r/M_s$  close to 0.5 at 4 K and continue to display single-domain properties at higher temperatures. The possibility that domain-wall formation is inhibited in these samples cannot be ruled out. Sample e26, however, has a maximum value of  $M_r/M_s = 0.82$ . Such high remanence values are possible in single-domain materials only if the degree of alignment is high and if the hysteresis loops are measured with the magnetic field parallel to the easy axes (Dunlop et al. 1993). Such a high degree of alignment is unlikely in polycrystalline pellets containing many individual grains, and hence we suggest that the hysteresis properties in e26 are governed by the motion of thin conventional domain walls that are strongly pinned by the fine-scale fluctuations in composition and stress.

### Implications for natural magnetic minerals

The most important carriers of NRM in rocks are the titanomagnetite solid solution ( $\text{Fe}_{3-x}\text{Ti}_x\text{O}_4$ ) and the titanohematite solid solution ( $\text{Fe}_{2-x}\text{Ti}_x\text{O}_3$ ), both of which have miscibility gaps at low temperature (Nord and Lawson 1989; Price 1981). Although microstructures associated with subsolvus exsolution are less common than microstructures associated with high-temperature oxidation,

Price (1980) noted that the extremely fine scale of these textures (usually resolvable only by using TEM) means that they are often overlooked in magnetic studies. Minerals that have been held at temperatures within the spinodal are unstable with respect to any fluctuation in composition. Even at temperatures above the spinodal the presence of a solvus can produce short-range clustering and fine-scale nonperiodic heterogeneities in composition or cation order. These fluctuations are a common feature of synthetic samples quenched from high temperatures (Harrison and Putnis 1995) and provide the template for spinodal decomposition at lower temperatures. Such precursor microstructures have been identified in synthetic clinopyroxene (Buseck et al. 1980). The very early stages of spinodal decomposition are therefore to be expected in natural magnetic minerals, and it is important to assess the magnetic consequences of such microstructures.

In the early stages of spinodal decomposition we observed very high remanence and coercivity only at temperatures below which the whole sample is magnetized. For this to have significance in nature, this temperature must be above room temperature. This condition would be easily satisfied in the titanomagnetite solutions because the  $T_c$  of the solid solution is above room temperature for compositions with  $y < 0.75$ – $0.8$  (Stephenson 1972). The solvus is approximately symmetrical with a consolute temperature  $< 490^\circ\text{C}$  (Price 1981). Therefore, titanomagnetites, which commonly have bulk compositions in the range  $0.5 < y < 0.6$ , pass through a high-coercivity state during the early stages of spinodal decomposition. At slightly higher temperatures the coercivity is lowered considerably by the development of paramagnetic boundary regions. This would allow the material to obtain a viscous magnetization (Dunlop 1990) in the presence of a small magnetic field by the movement of interaction-domain walls. This magnetization would stabilize at lower temperatures because of the interaction-domain to conventional-domain transition. Unusual viscous magnetization behavior in apparently single-phase, stoichiometric, multidomain titanomagnetite has been the source of much debate (Dunlop 1990; Deutsch et al. 1981). Deutsch et al. (1981) suggested that these properties result from suboptical subdivision of multidomain grains, although this was not confirmed by TEM investigation, and the mechanism of subdivision was not discussed.

Clearly, useful analogies can be drawn between the magnetite-spinel and titanomagnetite solid solutions. We now have the opportunity to study the behavior of magnetite-bearing solid solutions during the very early stages of exsolution and clustering using well-characterized material. The occurrence of such microstructures in natural and synthetic minerals needs to be confirmed by increased use of TEM as a routine characterization technique. The important role of compositional fluctuations in controlling magnetic properties means it is no longer sufficient to state that a mineral is single-phase on the basis of optical or SEM investigation alone. Experimental studies of the interaction between magnetism and microstructure are important but tend to raise more questions

than they answer regarding the nature of the interaction and the detailed domain-wall structure. A theoretical understanding is now required. Spinodal decomposition in cubic minerals is an ideal starting point for theoretical modeling because the geometry, wavelength, and amplitude of compositional fluctuations are well constrained. Quantitative analysis, however, will only be achieved by determination of the key magnetic parameters as a function of temperature and composition.

### ACKNOWLEDGMENTS

Low-temperature magnetic hysteresis loops were recorded at the Interdisciplinary Research Centre in Superconductivity, Cambridge. R.J.H. thanks Charles Dewhurst for his help in making the measurements. The authors thank R. Merrill and an anonymous reviewer for their comments on the manuscript. High-temperature susceptibility measurements were made at the Institute for Rock Magnetism (IRM), Minneapolis, with the aid of a grant from the University of Minnesota. R.J.H. thanks the IRM for the use of its facilities and Chris Hunt for his help in performing the experiments. The IRM is funded by the Keck Foundation, the National Science Foundation, and the University of Minnesota. R.J.H. acknowledges the receipt of a grant from the Natural Environment Research Council.

### REFERENCES CITED

- Banfield, J.F., Wasilewski, P.J., and Veblen, D.R. (1994) TEM study of relationships between the microstructures and magnetic properties of strongly magnetized magnetite and maghemite. *American Mineralogist*, 79, 654–667.
- Bates, L.F., Craik, D.J., and Isaac, E.D. (1962) Domain structures and coercivity of Alcomax III. *Proceedings of the Physical Society*, 79, 970–976.
- Brown, N.E., Navrotsky, A., Nord, G.L., Jr., and Banerjee, S.K. (1993) Hematite-ilmenite ( $\text{Fe}_2\text{O}_3$ - $\text{FeTiO}_3$ ) solid solutions: Determinations of Fe-Ti order from magnetic properties. *American Mineralogist*, 78, 941–951.
- Buseck, P.R., Nord, G.L., Jr., and Veblen, D.R. (1980) Subsolidus phenomena in pyroxenes. In *Mineralogical Society of America Reviews in Mineralogy*, 7, 117–211.
- Carpenter, M.A., Powell, R., and Salje, E.K.H. (1994) Thermodynamics of nonconvergent cation ordering in minerals: I. An alternative approach. *American Mineralogist*, 79, 1053–1067.
- Craik, D.J., and Isaac, E.D. (1960) Magnetic interaction domains. *Proceedings of the Physical Society*, 76, 160–162.
- Deines, P., Nafziger, R.H., Ulmer, G.C., and Woermann, E. (1974) Temperature-oxygen fugacity tables for selected gas mixtures in the system C-H-O at one atmosphere total pressure. Pennsylvania State University, College of Earth and Mineral Sciences, *Bulletin of the Experimental Station*, 88, 129.
- Deutsch, E.R., Pätzold, R.R., and Radhakrishnamurty, C. (1981) Apparent superparamagnetic behavior of some coarse-grained synthetic titanomagnetite. *Physics of the Earth and Planetary Interiors*, 26, 27–36.
- Dieckmann, R. (1982) Defects and cation diffusion in magnetite: IV. Non-stoichiometry and point defect structure of magnetite ( $\text{Fe}_{3-x}\text{O}_4$ ). *Berichte Bunsengesellschaft Physikalische Chemie*, 86, 112–118.
- Dieckmann, R., and Schmalzried, H. (1977) Defects and cation diffusion in magnetite (II). *Berichte Bunsengesellschaft Physikalische Chemie*, 81, 414–419.
- Dunlop, D.J. (1974) Thermal enhancement of magnetic susceptibility. *Journal of eophysics*, 40, 439–451.
- (1981) The rock magnetism of fine particles. *Physics of the Earth and Planetary Interiors*, 26, 1–26.
- (1990) Developments in rock magnetism. *Reproductions of Progress in Physics*, 53, 707–792.
- Dunlop, D.J., Xu, S., Özdemir, Ö., AlMawlawi, D., and Moskovits, M. (1993) Magnetic properties of arrays of oriented iron particles as a function of particle size, shape and spacing. *Physics of the Earth and Planetary Interiors*, 76, 113–121.
- Evans, M.E., and Wayman, M.L. (1974) An investigation of the role of ultra-fine titanomagnetite intergrowths in paleomagnetism. *Geophysical Journal of the Royal Astronomical Society*, 36, 1–10.
- Graham, J.W. (1953) Changes in ferromagnetic minerals and their bearings on magnetic properties of rocks. *Journal of Geophysical Research*, 58, 243–260.
- Hargraves, R.B., and Banerjee, S.K. (1973) Theory and nature of magnetism in rocks. *Annual Review of Earth and Planetary Sciences*, 1, 269–296.
- Harrison, R.J., and Putnis, A. (1995) Magnetic properties of the magnetite-spinel solid solution: Saturation magnetization and cation distributions. *American Mineralogist*, 80, 213–221.
- (1996) Magnetic properties of the magnetite-spinel solid solution: Curie temperatures, magnetic susceptibilities, and cation ordering. *American Mineralogist*, 81, 375–384.
- Hilliard, J.E. (1970) Spinodal decomposition. In H.I. Aaronson, Ed., *Phase transformations*, p. 497–560. American Society for Metals, Ohio.
- Hirsch, P.B., Howie, A., Nicholson, R.B., and Pashley, D.W. (1965) Electron microscopy of thin crystals, p. 317–352. Butterworths, London.
- Krasnova, N.I., and Krezer, Y.L. (1995) New data on the nature of fine and ultrafine lamellae in titanomagnetite. *European Journal of Mineralogy*, 7, 1361–1372.
- Larson, E., Ozima, E., Nagata, T., and Strangway, D. (1969) Stability of remanent magnetization of rocks. *Geophysical Journal of the Royal Astronomical Society*, 17, 263–292.
- Lehmann, J., and Roux, J. (1986) Experimental and theoretical study of  $\text{Fe}^{2+}$ ,  $\text{Mg}$ /( $\text{AlFe}^{3+}$ ) $_2\text{O}_4$  spinels: Activity-composition relationships, miscibility gaps, vacancy contents. *Geochimica et Cosmochimica Acta*, 50, 1765–1783.
- Livingston, J.D. (1981) Microstructure and coercivity of permanent-magnet materials. *Progress in Materials Science*, 41a, 243–267.
- McLaren, A.C. (1991) Transmission electron microscopy of minerals and rocks, p. 181–184. Cambridge University Press, Cambridge.
- Melnikov, B.N., and Khisina, N.R. (1976) Spinodal decomposition and related partial self-reversal of magnetization in titanomagnetite from the rift zones of Africa. *Earth Physics*, 10, 84–92.
- Merrill, R.T., and Halgedahl, S.L. (1995) Theoretical and experimental studies of magnetic domains. *Reviews of Geophysics*, 33, 137–144.
- Nafziger, R.H., Ulmer, G.C., and Woermann, E. (1971) Gaseous buffering for the control of oxygen fugacity at one atmosphere pressure. In G.C. Ulmer, Ed., *Research techniques for high pressure and high temperature*, p. 9–41. Springer-Verlag, New York.
- Nell, J., and Wood, B.J. (1989) Thermodynamic properties in a multicomponent solid solution involving cation disorder:  $\text{Fe}_3\text{O}_4$ - $\text{MgFe}_2\text{O}_4$ - $\text{FeAl}_2\text{O}_3$ - $\text{MgAl}_2\text{O}_4$  spinels. *American Mineralogist*, 74, 1000–1015.
- Newell, A.J., Dunlop, D.J., and Williams, W. (1993) A two-dimensional micromagnetic model of magnetizations and fields in magnetite. *Journal of Geophysical Research*, 98, 9533–9549.
- Nord, G.L., Jr., and Lawson, C.A. (1989) Order-disorder transition-induced twin domains and magnetic properties in ilmenite-hematite. *American Mineralogist*, 74, 160–176.
- O'Neill, H.St.C., and Navrotsky, A. (1983) Simple spinels: Crystallographic parameters, cation radii, lattice energies, and cation distribution. *American Mineralogist*, 68, 181–194.
- Price, G.D. (1980) Exsolution microstructures in titanomagnetites and their magnetic significance. *Physics of the Earth and Planetary Interiors*, 23, 2–12.
- (1981) Diffusion in the titanomagnetite solid solution series. *Mineralogical Magazine*, 44, 195–200.
- Putnis, A. (1992) *Introduction to mineral sciences*, 457 p. Cambridge University Press, Cambridge.
- Sack, R.O., and Ghiorso, M.S. (1991) An internally consistent model for the thermodynamic properties of Fe-Mg-titanomagnetite-aluminate spinels. *Contributions to Mineralogy and Petrology*, 106, 474–505.
- Shive, P.N., and Butler, R.F. (1969) Stresses and magnetostrictive effects of lamellae in the titanomagnetite and ilmenohematite series. *Journal of Geomagnetism and Geoelectricity*, 21, 781–796.
- Smith, P.P.K. (1980) Spinodal decomposition in a titanomagnetite. *American Mineralogist*, 65, 1038–1043.
- Stephenson, A. (1972) Spontaneous magnetization curves and curie points

- of spinels containing two types of magnetic ion. *Philosophical Magazine*, 25, 1213–1232.
- Strangway, D.W., Larson, E.E., and Goldstein, M. (1968) A possible cause of high magnetic stability in volcanic rocks. *Journal of Geophysical Research*, 73, 3787–3795.
- Tucker, P., and O'Reilly, W. (1980) The laboratory simulation of deuteric oxidation of titanomagnetites: Effect on magnetic properties and stability of thermoremanence. *Physics of the Earth and Planetary Interiors*, 23, 112–133.
- Wood, B.J., Kirkpatrick, R.J., and Montez, B. (1986) Order-disorder phenomena in  $\text{gAl}_2\text{O}_3$  spinel. *American Mineralogist*, 71, 999–1006.
- Worm, H.U., Ryan, P.J., and Banerjee, S.K. (1991) Domain size, closure domains, and the importance of magnetostriction in magnetite. *Earth and Planetary Science Letters*, 102, 71–78.
- Xu, S., and Merrill, R.T. (1989) Microstress and microcoercivity in multidomain grains. *Journal of Geophysical Research*, 94, 10627–10636.
- Zijlstra, H. (1982) Permanent magnets: Theory. In E.P. Wohlfarth, Ed., *Ferro-magnetic materials: A handbook of the properties of magnetically ordered substances*, p. 27–105. North-Holland, Amsterdam.

MANUSCRIPT RECEIVED JANUARY 23, 1996

MANUSCRIPT ACCEPTED OCTOBER 16, 1996